HADES experimental setup: modernization of electronics and data analysis (Student Team Project 2, group 4)

Agata Otręba, Piotr Piotrowski, Aleksandra Podwysocka,
Marcel Półkośnik, Damian Sokulski

April 4, 2024

Abstract

In November 2023 a group of students from Faculty of Physics of University of Warsaw visited the GSI facility to familiarize themselves with detectors and technologies used by the HADES collaboration. Besides learning we helped to upgrade the MDC and ECAL detectors for the heavy-ion experiment planned for 2024. In this report the HADES setup is described with focus on the mentioned subdetectors. We also report on the work done by the group. Also we visited the selected GSI facilities which are described in this report.

Contents

Acknowledgements

We thank dr hab. Krzysztof Piasecki, dr hab. Krzysztof Turzyński, dr hab. Piotr Nieżurawski, mgr Jan Kollarczyk, mgr Antonin Opichal, dr Adrian Rost, dr Christian Wendisch, dr Christian Müntz, dr Małgorzata Gumberidze, dr Alexandre Gumberidze, dr hab. Piotr Gasik, mgr Michał Mikołajczuk, dr Hartmut Vormann, Sebastian Schall, prof. Joachim Stroth, dr Pavel Tlusty, mgr Joanna Papierska for making this project possible.

1 Introduction

This report summarizes the trip of 5 students to GSI Helmholtzzentrum für Schwerionenforschung in Darmstadt, Germany, that includes some experimental work at HADES (The high-acceptance di-electron spectrometer) and visits to several research facilities on place. The trip took place between 30.10.2023 and 3.11.2023.

The main purpose of HADES is to investigate physics of relativistic heavy-ion reactions. During the visit our task was to help in upgrading and commissioning of two detectors of the HADES system for the next ion beam planned for first half of 2024.

The GSI also hosts the SchwerIonenSynchrotron 18 (SIS18) accelerator since decades and currently is a construction site of SIS100 accelerator.

1.1 HADES experimental setup

HADES is divided into six hexagonally symmetric sectors surrounding the beam axis. The detector is composed of subsystems designed for specific purposes (scheme shown in Figure 1). The innermost detector is Ring Imaging Cherenkov (RICH) filled with hadron-blind gas for identification of relativistic electrons and muons. Four stations of Mini-Drift Chambers (MDC) are responsible for tracking particles and momentum reconstruction of charged hadrons. In the middle of the MDC stations a superconducting magnet is installed that aims at bending charged particles. A Time of Flight measurement system installed downstream, is composed of two detectors: Resistive plate chambers (RPC) and TOF. The new detector, Electromagnetic Calorimeter (ECAL) was added in 2017. It aims at measuring energy of photons and electrons, which allows to study new reaction channels of heavy ion collisions.

During the visit in GSI our work on upgrading HADES was focused on the MDC and ECAL subdetectors. For this reason these detectors are described in more details in the following subsections.

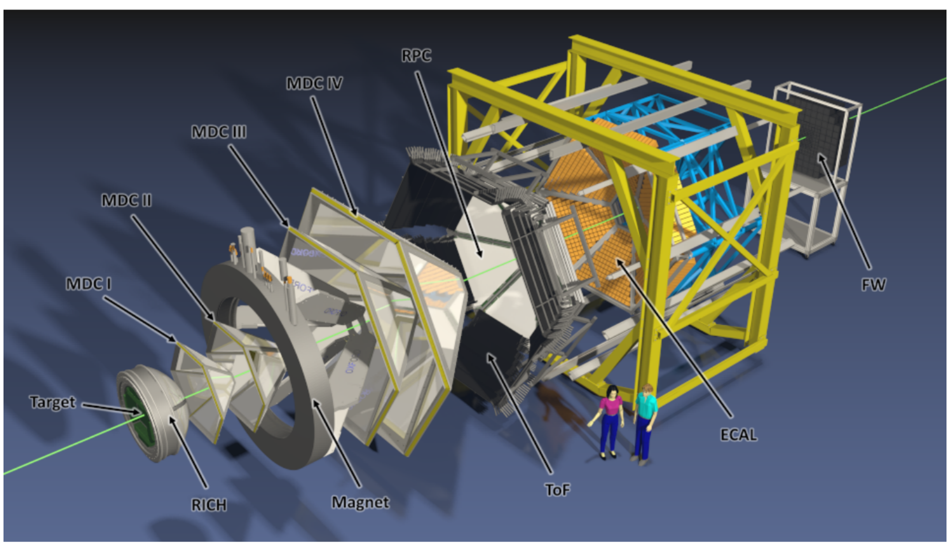

Figure 1: Scheme of HADES detector experimental setup [1].

1.2 Structure of ECAL

ECAL is a device that aims at direct detection of photons and measurement of their energy. The calorimeter installed at HADES setup is over 4.5 m wide and divided into 6 trapezoidal sectors. Each of those sectors consists of 163 modules (see Figure 2). The trapezoids are arranged in such a way, that the azimuthal angle is almost fully covered and for polar angles the proposed coverage is between 12° and 45° [3]. Figure 2 also shows the frame in which ECAL is placed. It provides access to all the modules from behind.

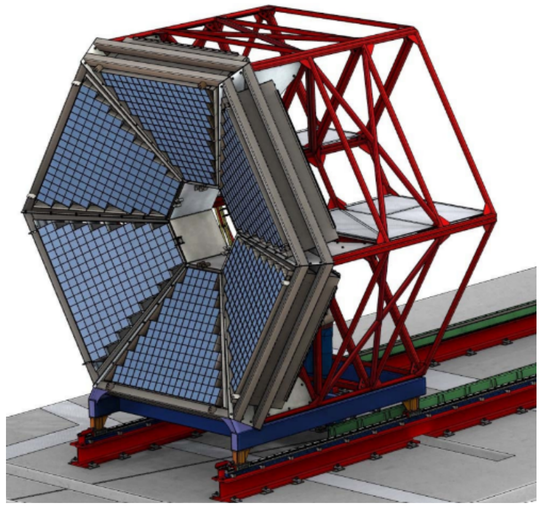

Figure 2: Layout of ECAL sectors [2].

Figure 3 shows the structure of a single ECAL module. The main part of each module is a lead glass prism acting as a Cherenkov radiator. Photons and electrons entering the module will create an electromagnetic shower. In the shower electrons and positrons are created and Cherenkov light will be emitted. The Cherenkov photons are detected by a photomultiplier tube. When a photon strikes photocatode, photoelectric effect occurs and in consequence photo-electrons are emitted. Then those electrons are directed towards dynodes of photomultiplier (PMT), where secondary emission takes place multiple times, resulting in exponential growth of number of electrons. The signal is then sent to further electronics.

PMT is placed in a magnetic shield, so that the residual magnetic field from HADES superconducting magnet coils does not affect electrons' tracks, what could result in loss of some particles from the cascade in between dynodes. The lead glass prism is covered by a brass envelope, whereas PMT with its shield is placed in an aluminum housing. Each module is connected to an optical fiber for a laser monitoring system (not shown in the Figure 3).

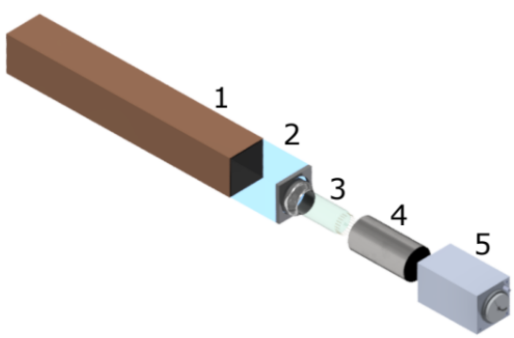

Figure 3: Structure of a single ECAL module; 1 - brass envelope, 2 - lead glass prism, 3 - photomultiplier, 4 - magnetic shield, 5 - aluminum housing for the photomultiplier and magnetic shield [3].

As shown in Figure 4, a signal from the photomultiplier of each module is then processed by PaDiWa-AMPS. It is a front-end-board of a TRB3 platform (3rd generation General Purpose Trigger and Readout Board), which performs a high precision time-to-digital conversion. Then the data collected is sent through the custom network structure TRBNet to the HADES data acquisition system - DAQ.

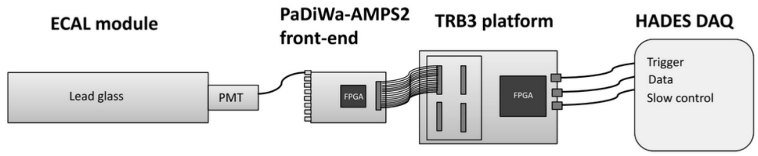

Figure 4: Simplified scheme of ECAL detector read-out [2]

The energy of a particle deposited in the lead glass element of an ECAL module is proportional to the charge of PMT signal, which needs a high accuracy measurement. To achieve this, a standard TOT (Time Over Threshold) measurement method[1] is modified to the charge-to-time-over-threshold (Q2TOT), where the charge of the PMT pulse is encoded in the width of a digital signal. This is carried out via the PaDiWa-AMPS, utilising two types of signals, see Figure 5. The FAST signal contains the information on time of arrival, while SLOW signal is used for an extraction of charge information.

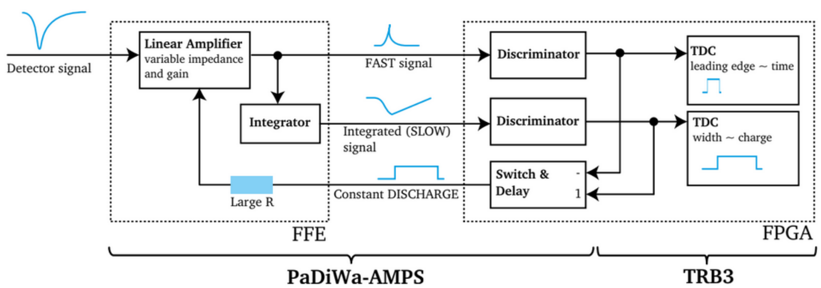

Figure 5: Signal processing in the PaDiWa-AMPS circuit [2]

1.3 Structure of MDC

Every drift chamber contains cathode-anode pairs. If a charged particle passes through the gas surrounding the electrodes it ionizes gas molecules, creating gas of free electrons and positively charged ions. Both electrons and ions start to drift towards the anodes and cathodes, respectively. Electrons approaching the cathode being accelerated by the rising electrical field and gain sufficient energy to cause the secondary ionization. This process generates an avalanche that multiplies the charge collected by an electrode by a factor up to several 10^4 [5], allowing further signal analysis.

To study the trajectory of a passing particle effectively, one needs many drift cells characterized by small granularity to aim for high resolution in position measurement. However, achieving a resolution of 100 µm demands more than just small granularity. A way to achieve this goal is by utilizing multi-wired drift chambers. The HADES Mini Drift Chambers (MDC) system is comprised of modules (see Figure 6), which are plates containing layers of wires, including cathodes and anodes, arranged in parallel. The space between these wires is filled with gas. When particles ionize this gas, the resulting ionized particles move towards the nearest electrodes, facilitating the precise measurement of their positions.

[1]Time duration of a signal over a threshold value rises monotonously with the charge collected

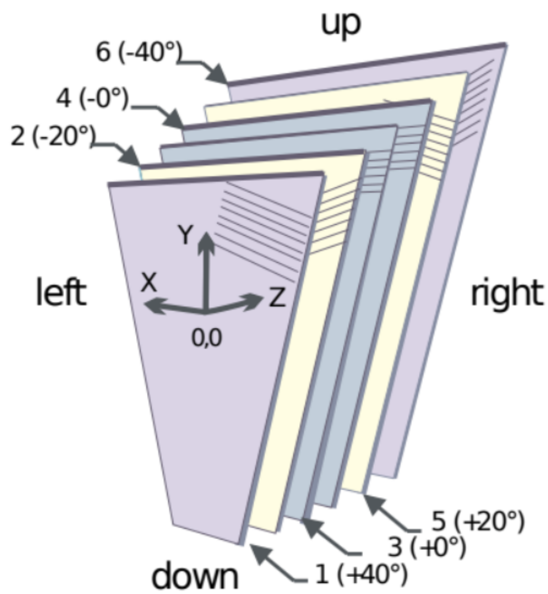

Figure 6: Arrangement of layers and orientation of wires in all the HADES drift chambers. The sketch omits the cathode layers [5].

The space between individual wires forms a single unit called a drift cell. By reading signals from various anode or sense wires that intersect in the transverse plane, we can indicate where the particle passed through (this is the point of intersection of the wires from which signals were received at the same time). The scheme of a single drift cell is presented in Figure 7.

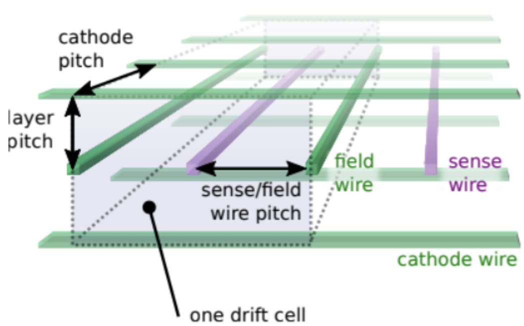

Figure 7: Visualisation of multiple drift cells using wires [5].

A single drift cell operates on the principle of a regular drift chamber. The signal is generated by charges, which are created after the passage of a traversing particle, hitting the appropriate electrode. A schematic drawing illustrating this situation is shown in the Figure 8.

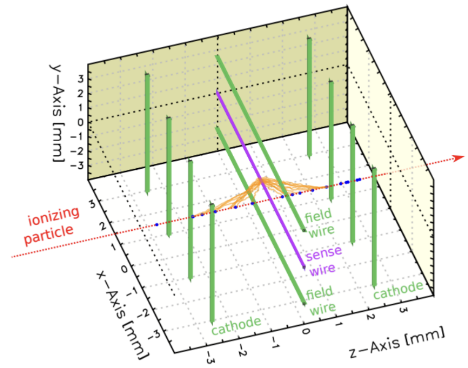

Figure 8: Sketch of particle passing through a single drift cell [5].

To get the data from all the MDC layers a number of 27000 [5] individual sense wires need to be read out. To achieve this goal, the custom Front End Electronics (FEE) is used. The input signal from each MDC layer is grouped in packs of 16 wires. Each pack is fed into one daugherboard containg pre-amplifier, signal shaper and discriminator. These parts are responsible for the sequential pre-processing of the analog input signal. Next, the signal is taken over by the respective motherboard containing the time to digital converter (TDC). Each motherboard has 4 or 6 daughterboards connected as shown in Figure 9. After conversion, the motherboard passes digital signal to further electronics, which are not part of the FEE.

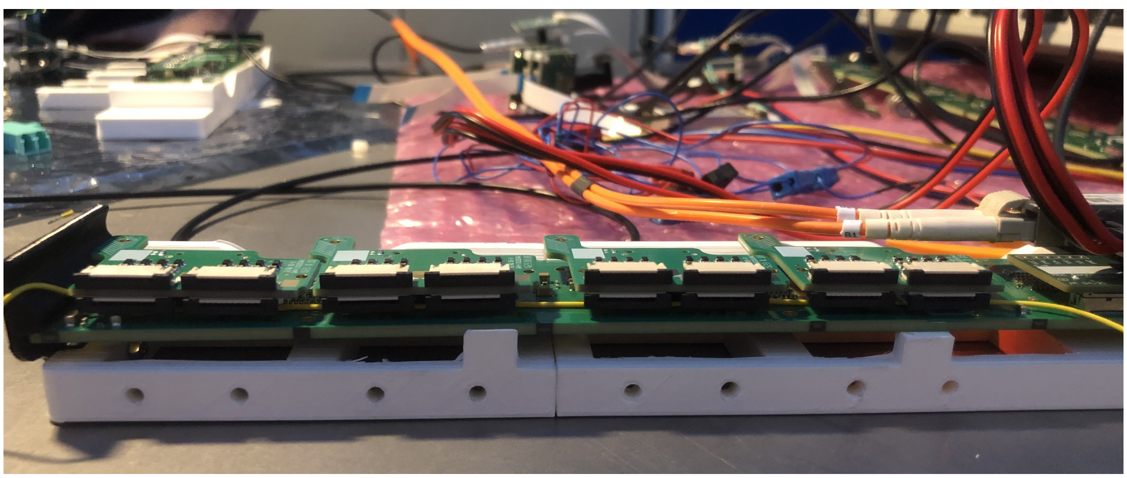

Figure 9: Photo of the daughterboards fixed on the motherboard.

2 Our contribution to upgrading and commisioning of HADES

2.1 Upgrading ECAL - Tests

We measured signals from PaDiWa-AMPS boards, using the oscilloscope. The signal was usually generated by muons from cosmic radiation, although we also used a laser diode. A typical output can be seen in figure 10. During the tests, we found one faulty PaDiWa-AMPS module, where the FAST signal was significantly delayed. This caused an inaccurate data read-out, thus the module had to be replaced.

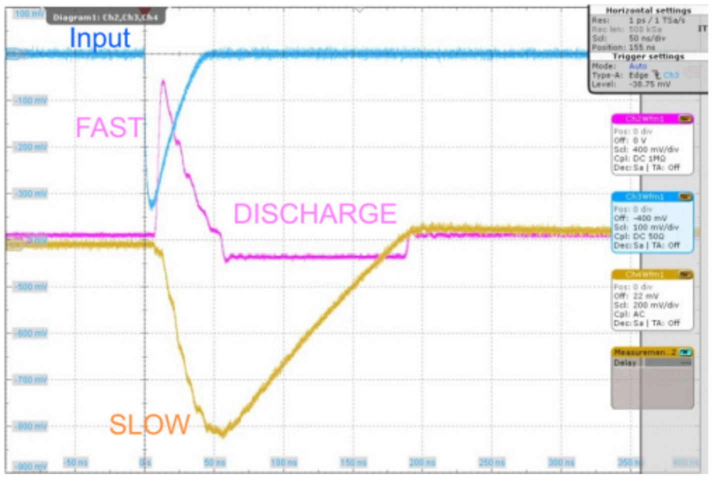

Figure 10: Signal from the PaDiWa-AMPS board measured by the oscilloscope. Input signal is shown in blue and output signals in yellow and magenta [2]

Another goal was to assess if the HV delivered to subsequent modules were chosen correctly and if the electronics worked properly. The tool to check it was the measurement of the cosmic radiation, where the position of signal amplitude was verified. We performed the measurement of the minima of negative signals from the ECAL PMT tubes for about 24 hours using the oscilloscope. The PMT signals were generated by cosmic muons. The number of muons and values of a minimum measurement of their signals were registered. An exemplary result is shown in figure 11, where the minimum is located around 300 mV. We collected the values of these minima in the histogram. Thus, we obtained the distribution counting 277 420 measurements of the signals from cosmic particles.

It is useful to process the scope data in ROOT. With the ROOT macro we imported the data from the oscilloscope and the result is shown in the histogram in figure 12.

We can also find a similar distribution of cosmic particles by using the PaDiWa-AMPS read-out system of ECAL. This system translates the amplitudes of PMT signals into the time width of the output signal. Such a histogram is shown in figure 13.

After the collected data was analysed, some changes in the electronics (for example switching a divider) were decided to be made.

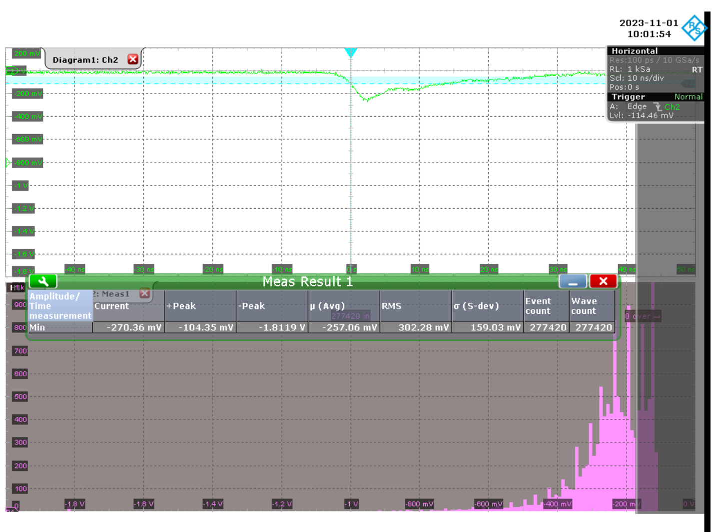

Figure 11: Scope screenshot for channel 2. The green line is the signal from a PMT. The pink distribution of amplitude below is the result of the long time measurement.

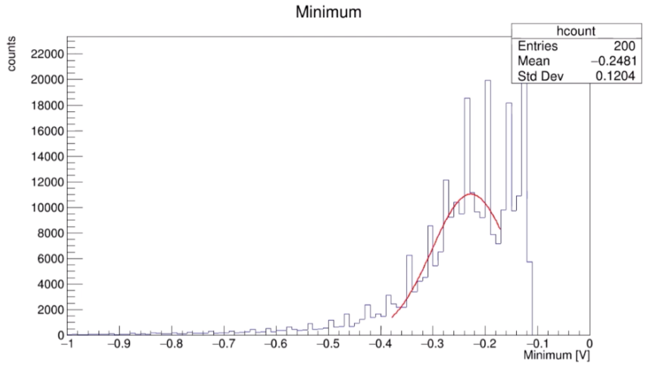

Figure 12: Histogram of amplitudes obtained within the long time measurement. Data reading and plotting by ROOT macro.

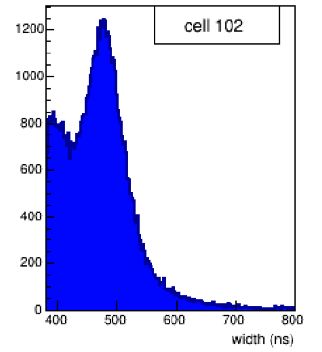

Figure 13: A histogram of the widths of the PaDiWa-AMPS output signal, where the PMT amplitudes are encoded.

At the end we did the laser test. The laser was emitting a light signal into the modules. In this case, our task was unplugging the optical fibers that are shown in figure 15 from each module and checking whether the signal was disappearing from the look-up table on the screen (Figure 14). We were verifying if the position of the specific module on the frame corresponds with the look-up table.

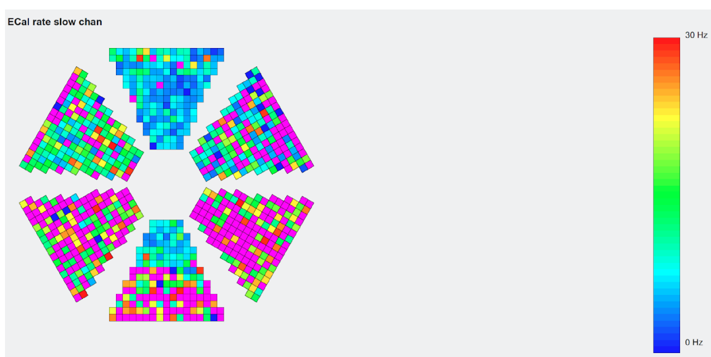

Figure 14: The look-up table containing an overview of modules with numbers and specific positions that are connected to PaDiWa boards. The signal rate is displayed for each module.

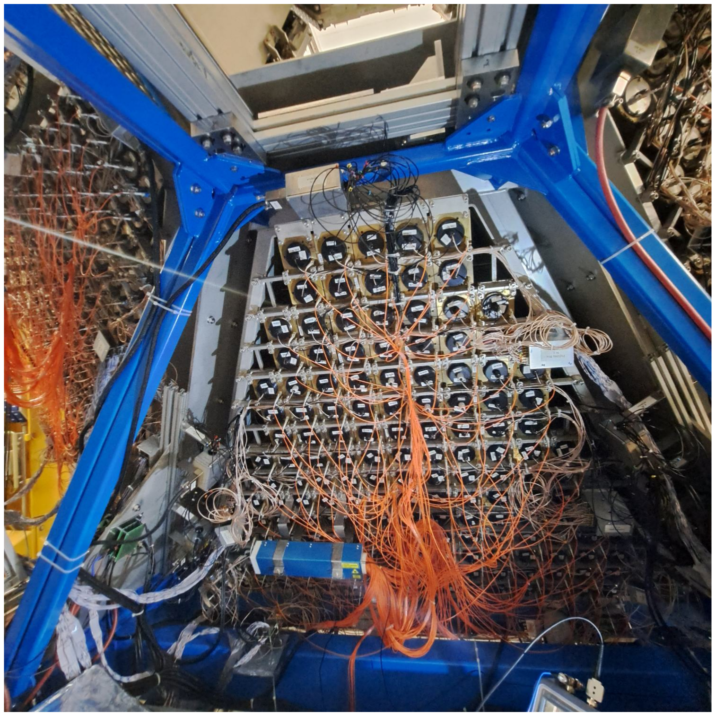

Figure 15: Photo of the single ECAL sector with its modules. The laser is located in the blue aluminum tube on the front. The optical fibers are the orange ones. They are connected to the optical fibers inside the module, through the connector in the brass plates on the module.

2.2 Upgrading MDC

Our task was to test as many newly produced daughterboards as possible. The first part of our work was to construct the testing setup.

To avoid time-consuming plugging of thin flex print cables we proved that the daughterboards can be tested by putting unshielded single core signal wire connected to an pulse generator right after the input connectors. We ended up having the motherboard with fixed signal emitting wire right under the daughterboard connectors and second signal emitting wire that we could manually put on the top of the daughterboards. That setup (shown on Figure 16) allowed us to quickly test 4 boards at the same time.

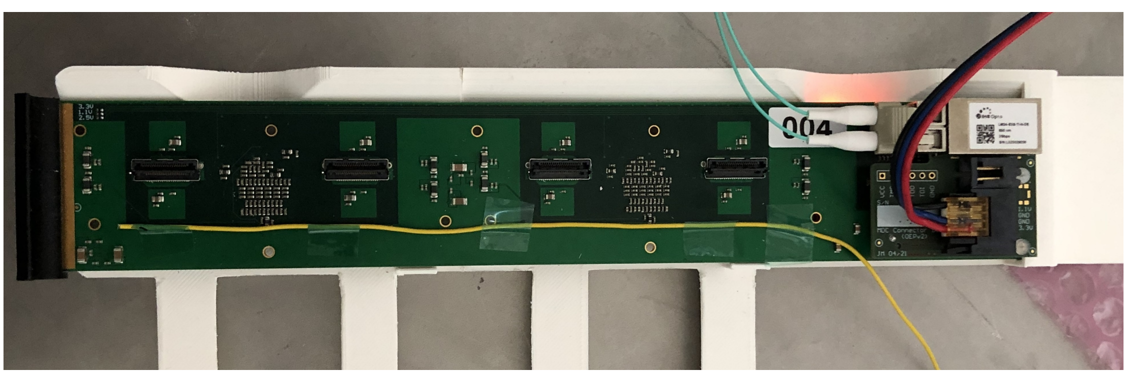

Figure 16: Photo of the daughterboards testing setup.

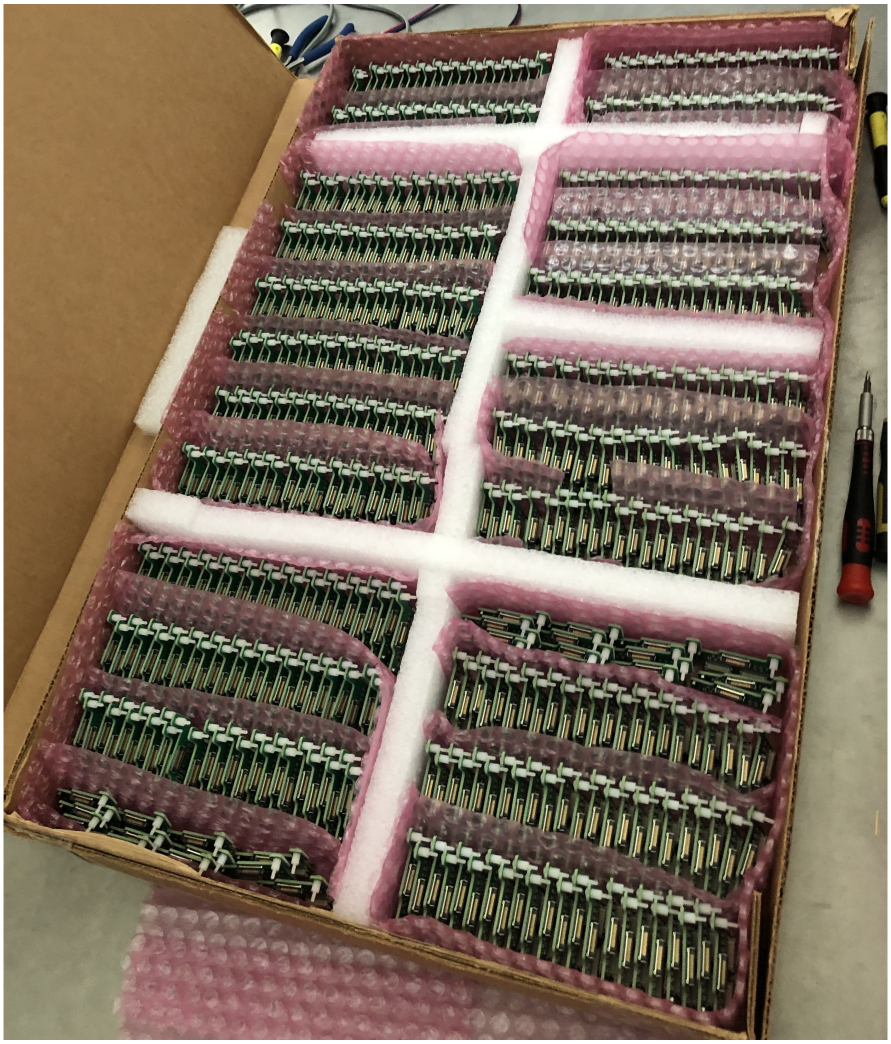

Figure 17: Box of daughterboards prepared and tested by our group.

To test the boards we used the dedicated Python and Bash scripts to display the signal strength from all the motherboard output channels. We assumed that a daughterboard works if all the channels register signal above a certain threshold.

We managed to test between 400 and 500 daughterboards, and found that only 4 of them were not working properly ($<$1 % of tested boards). In each of those cases only one of 16 channels on the board had no signal. We left them for further investigation on the site.

Beside testing, we also prepared over 900 daughterboards (see Figure 17) to attach them to motherboards in the final setup by installing fixing screws.

3 Our visits to the GSI facilities

Beside working on MDC and ECAL, our group visited various GSI facilities to familiarize ourselves with different technologies and solutions used on site.

3.1 Cleanroom

Cleanrooms, also known as clean laboratories, are a crucial component in research institutions specializing in particle physics and nuclear physics. Also GSI hosts such a specially designed facility. Inside the clean room, very high standards of air purity and environmental hygiene are maintained.

Their main purpose is to provide a controlled working environment, free from contaminants that could interfere with complex experiments conducted at the microscopic scale.

In clean rooms, air cleanliness levels are controlled, solid particles and foreign substances are removed, and humidity and temperature are monitored. This allows for maintaining stable environmental conditions necessary for precise measurements and experiments. Additionally, clean laboratories are often equipped with specialized equipment and tools, such as workstations, electron microscopes, or surface cleaning devices, enabling complex operations to be carried out at a very high level of cleanliness.

3.1.1 Standards

Cleanrooms adhere to specific ISO standards and all parameters are under strict control. One of the most important is the quantity of suspended solid particles in the air, determined by ISO 14644 norm. Limits for particle quantity are defined based on the size of particles. According to this standard, there are nine classes of air cleanliness, from ISO9 – the "dirtiest" to ISO1 – the "cleanest".

Depending on the required cleanliness of the atmosphere, clean rooms are divided into classes, and the quantity and size of pollutants are defined per cubic meter or cubic foot of air. At GSI, the typical ISO value of the quantity of suspended solid particles in the air is 10 000, but with specific rules, it is possible to achieve 100 solid particles, which is two orders of magnitude lower.

Figure 18: The view of the cleanroom and typical protective clothing and accessories required in it.[33][34]

Cleanrooms are separated from the external environment by appropriate building elements. Air is delivered into the interior using special air-filtering units. The key part of the filtration system is HEPA filters, through which air is pushed into the room. A special filter system captures subsequent fractions of contaminants. Elements are delivered to the cleanroom through special material sluices known as transfer windows. The flow path for personnel is strictly defined and passes through specially designed personnel airlocks.

GSI cleanroom is essential for conducting precise experiments, where even the slightest impurities can have a significant impact on the results. It is used in the production, assembly, and testing of delicate particle detector elements, electronic systems, and other advanced devices used in particle and nuclear physics research.

3.2 ESR

An important component of the experimental infrastructure at GSI is the Heavy Ion Storage Ring, hereafter referred to as ESR, an acronym for Experimental Storage Ring. Its tasks include storing and accumulating ions in such a way as to obtain the highest possible current.

Narrow velocity distribution and small beam divergence of ions can be achieved by three basic techniques. Each of them operates on different scales of precision:

- **Stochastic beam cooling** is the most general method. This means that it is a basic method and others improve its effectiveness. It works by applying electrical signals triggered by individual particles passing through a feedback loop. The goal, as with the other methods, is to reduce the tendency of particles to diverge from the initial direction [12]
- **Electron cooling** is a method that uses a parallel beam of electrons to obtain the desired heavy ion beam characteristics. An electron cooling beam is introduced into one of the straight parts of a storage ring. Its mean velocity and magnitude are equal to that of the heavy particle beam. Energy exchange between two kinds of particles is achieved by Coulomb scattering. If the electron beam is monochromatic enough and the particle trajectories are parallel to each other, the electron beam will play the role of an effective cooler, absorbing the energy from the heavy ion beam. [11]
- **Laser cooling** is a method that can improve the uniformity of the beam to an extent unattainable with other methods. At its core, this method involves the interaction between laser beams and atoms or ions. The laser force results from the scattering (absorption followed by emission) of laser photons from an ion. The absorbed photons come from a single direction and thus their contributions to momentum can only add along the laser line. The case is different for emissions, which can take place isotropically. Averaging these emissions balance each other out. [10]

In addition, the ESR is the place of accurate measurements of ion masses. Depending on the temperature of the beam, two methods of mass measurement are used. A first one, called Schottky Mass Spectrometry, determines the mass of a particle from pick-up signals induced by cooled ions traveling at almost the same velocity. Masses of hot ions with wider velocity distribution can be measured using the time-of-flight signals in the Isonchronous Mass Spectrometry. [7] [8]

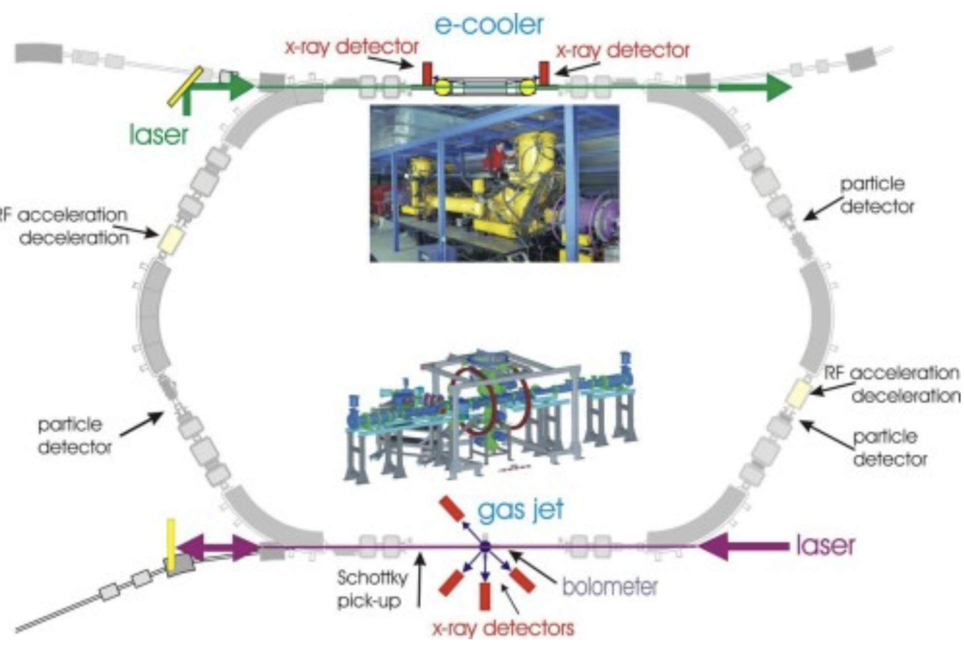

Figure 19: Construction scheme of Experimental Storage Ring [7]

Figure 20: A side view of the Experimental Storage Ring. A large number of measurement apparatus components and coolers obscure the beam path

3.3 FAIR

Currently the Facility for Antiproton and Ion Research (FAIR) as one of the largest research projects worldwide, is being built in Darmstadt. We had an opportunity to visit the construction site. New buildings will host the number of experiments on beams from the existing SIS18 accelerator and SIS100 synchrotron, the latter being built currently.

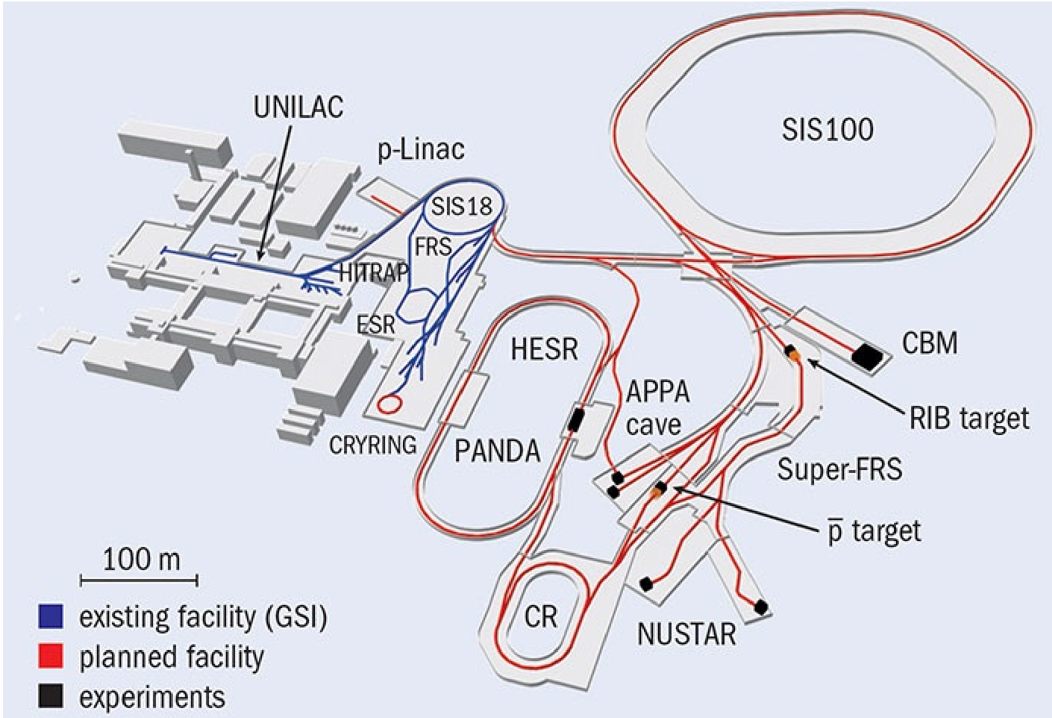

Figure 21: Scheme of the currently existing and planned buildings [14].

During our visit on-site we explored the new cave, where both HADES and CBM detectors would be mounted. The cave is placed close to the crossing of the beams from SIS18 and SIS100, but both detectors will receive a beam only from the SIS100.

In the new cave the CBM detector will stand behind HADES and during its operation, the beam might be stopped by the dump upstream from CBM. In the new setup (showed in Figure 22), two parts of CBM: the Ring Imaging Cherenkov (RICH) and Muon Chamber (MuCh) will be mounted on the tracks perpendicular to the beam axis. During muon measurements MuCh will be inserted in the place of RICH. Despite the fact that the cave is still under construction parts of the CBM are already being tested, and the tests are conducted on mini-CBM site or placed alongside the current HADES setup. All these systems are planned to allow CBM to work on extremely high interaction rate up to 10 MHz [15].

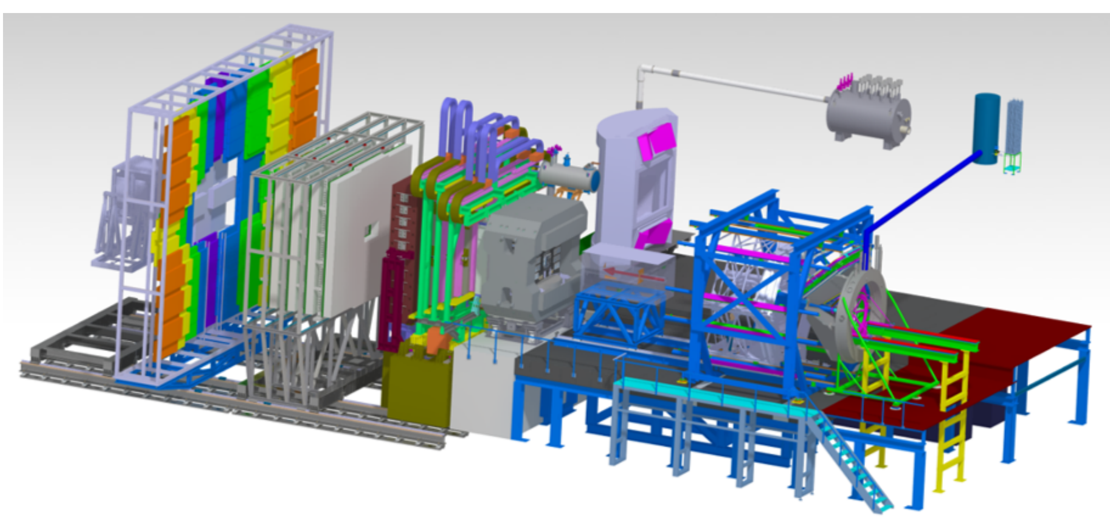

Figure 22: Scheme for HADES (right) and CBM (left) setups[16].

We also explored the place where the new Superconducting FRagment Separator (Super-FRS) will be built. The new two-stage fragment separator will focus on production, separation and identification of exotic nuclei that will be send to the storage ring or to dedicated experiments. An operation of both stages is based on the combination of magnetic bending and energy loss in a specially shaped degrader. Behind the separator target, the beam-catcher is mounted in order to get rid of primary beam ions which do not react with the target. Due to high radiation levels, both target and beam-catcher will be mounted in a highly shielded area. A built-in detector system will allow a fragment identification on an event-by-event basis and provide this information to the subsequent experiments. A schematics of Super-FRS is shown in Figure 23.

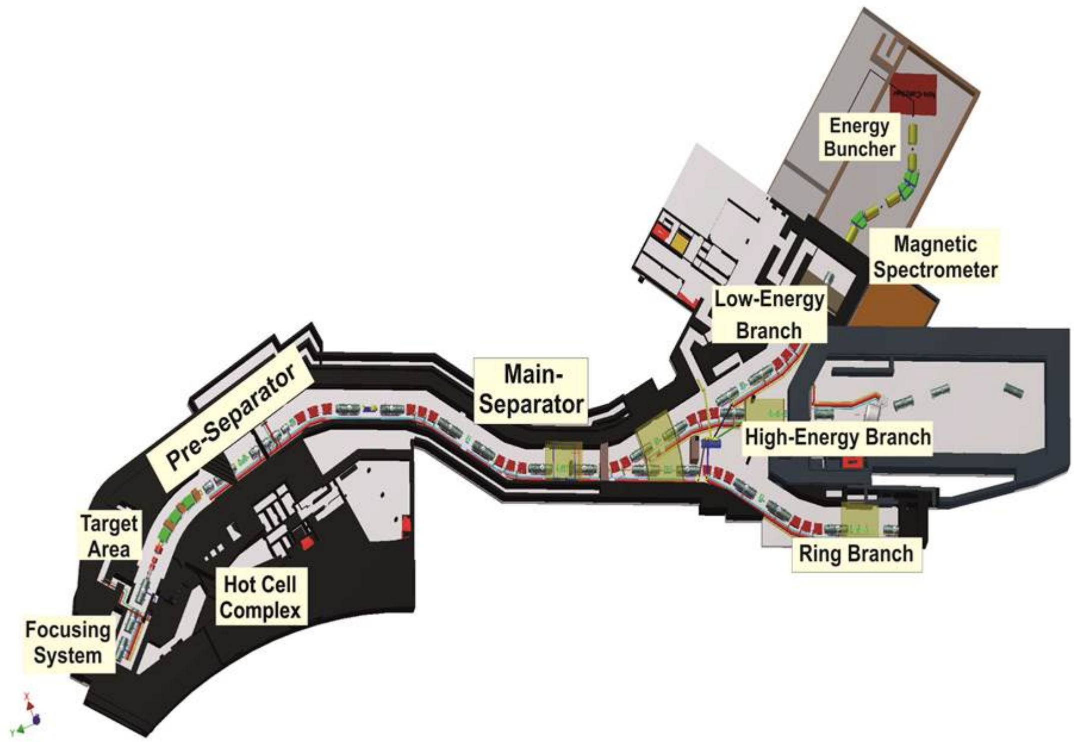

Figure 23: Scheme of planned Super-FRS [17].

Behind the Super-FRS further experiments using a beam of unstable nuclei will be conducted. These include:

- PANDA (antiProton ANnihilation at DArmstadt), focused on collisions of antiprotons with target inside a dedicated detector. In order to deliver the antiproton beam, the High-Energy Storage Ring (HESR) will gather them from the Super-FRS, where they are created and separated from the rest of the beam.
- APPA (Atomic Physics, Plasma and Applied sciences) focused on material science.
- NUSTAR (Nuclear Structure, Astrophysics and Reactions) focused on experiments investigating limits of stability, nuclear structure models, neutron matter and strong interactions, by using beams of rare radioactive nuclei from Super-FRS.

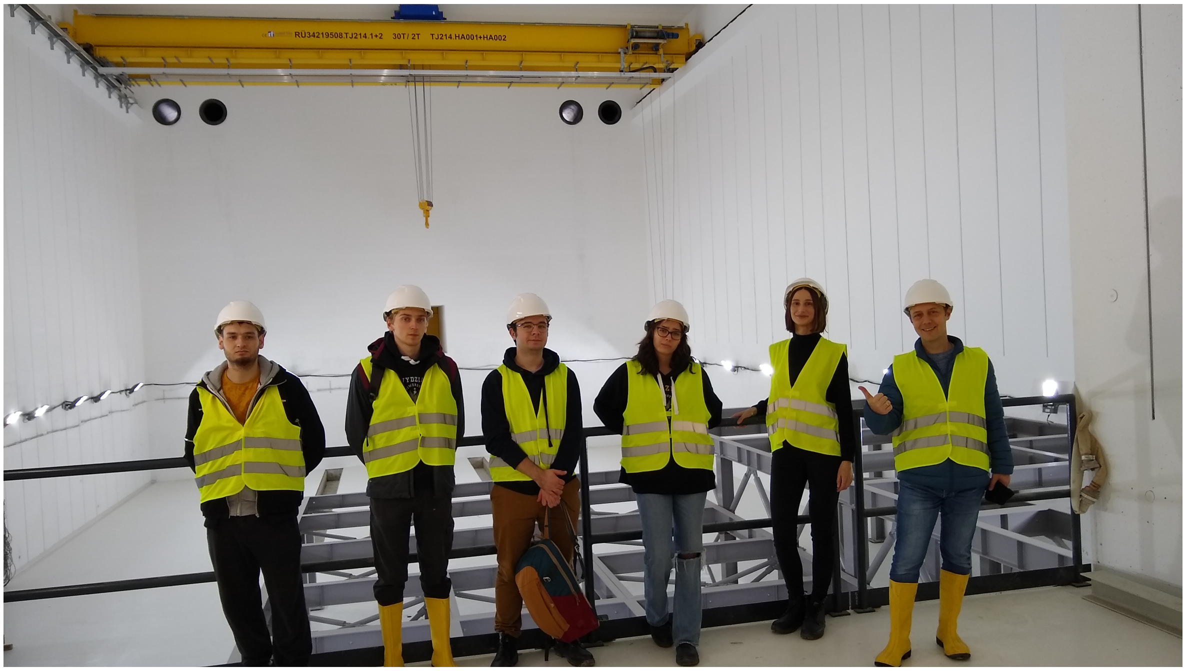

Figure 24: Our group inside the new HADES-CBM cave inside FAIR construction site.

3.4 Green IT Cube

A 12 million euro investment commissioned in 2016, Green IT Cube [18] shown in Fig. 25 is the main data centre at GSI, whose main purpose is to process and store experimental data and to perform various simulations, for example during development of new detectors. The data center consists of a main 6-level building, that can store up to 768 2.2 meters high racks, and a smaller supply building housing the cooling pumps.

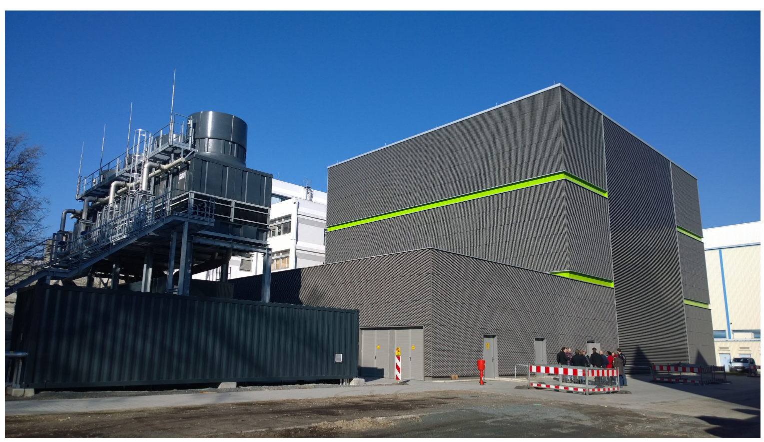

Figure 25: The building of Green IT Cube

At the moment, the data center features 600 nodes amounting to impressive 54 thousand CPU cores and 400 GPUs, with storage capacity of 60 petabytes. Green IT Cube is organized in a cluster of cores named Virgo 2 [19]. It provides a batch farm for processes managed by the SLURM scheduler. The cluster is connected by the InfiniBand network, which is a high-bandwidth and low-latency optimized High Performance Interconnect (HPI). Topology of the network is a flat tree. It allows for optimal usage of redundant connections with high-throughput. In following years further development of the facility is planned, parallel to the construction of FAIR, making the total cost of investment 21 million euro, raising the storage capacity to 250 petabytes and reaching transmission speeds greater than

1 terabyte per second. While being one of the most powerful in the world, Green IT Cube is also extremely efficient with PUE < 1.07 (Power Usage Effectiveness), which means that only up to 7% of electricity is used on cooling; in conventional data centers that number varies between 30% and 100%. Main reason of the state of the art efficiency is the innovative water cooling system, pumping 1150 cubic meters per hour, using 4 megawatts of power for every two levels, which is planned to be raised to 12 megawatts at the final construction. Additionally, the waste heat is utilized for heating offices and canteen building.

Figure 26: Our trip to the Green IT Cube

3.5 Ion-Beam Radiotherapy

One of the research areas conducted at GSI is the heavy ion-beam radiotherapy. Today, GSI is considered a pioneer in this technology. The research began at the institute 25 years ago using ^{12}C ions with an energy range of 80–430 MeV/u from the SIS-18 synchrotron and an innovative raster scanning system for the beam delivery. Over time, clinical studies were transferred to University Medical Center in Heidelberg to provide access to therapy for a bigger group of patients. So far, GSI has conducted numerous heavy ion radiotherapy procedures, treating patients with various types of tumors. The indications primarily included inoperable and radioresistant tumors of the skull base and neck.

3.5.1 Properties of Ion Beams

The primary goal of radiotherapy is to damage the largest possible tumor area while minimizing harm to healthy tissues. Therefore, tumors located in hard-to-reach areas require exceptional precision of the beam. This precision can be achieved by using either ions or hadrons. Carbon ions, as charged particles, possess specific characteristics that significantly differentiate them from the more commonly used photons. This stems from the specific interaction mechanisms with matter, which is different for each type of radiation. In case of photons, electromagnetic interaction occurs with processes such as electron ionization and electron-positron pair production, causing the photon to lose energy evenly along its entire path. On the other hand, charged particles interacting with matter cause electron density to increase at the end of their path, resulting in the formation of the characteristic Bragg peak. As a result, we observe a completely different distribution of deposited energy for both types of radiation, as seen in left panel of Figure 27.

For hadrons or ions, ionization of the medium is the highest in the Bragg peak region, allowing a favorable dose distribution at a specific depth with very small scattering angles. Immediately after, the dose value drops rapidly, almost to zero. Consequently, healthy tissues around the tumor can be very well protected as seen in the right panel in Figure 27. This also translates into biological effectiveness.

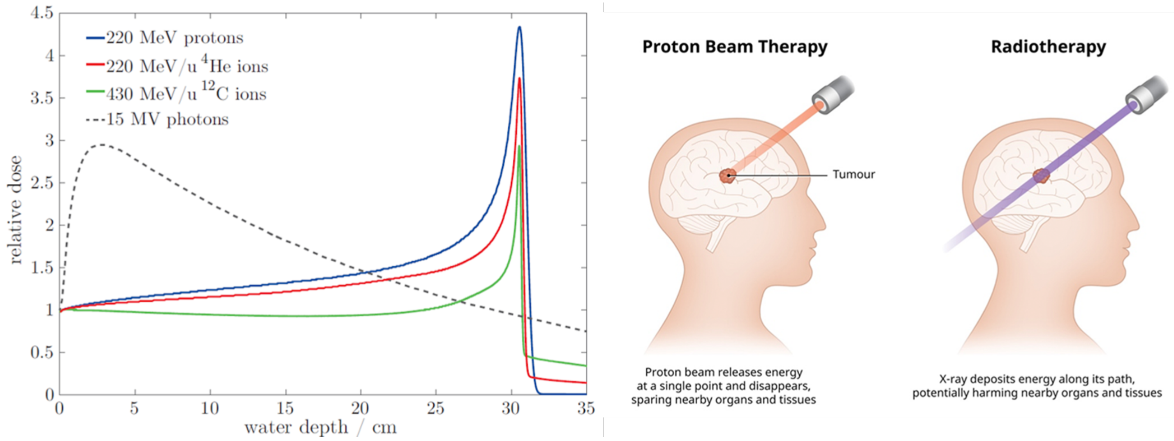

Figure 27: Dose distribution for various types of radiation (left) and visualization of the passage through tissues by proton (and ion) beams vs. photon beam (right).[27][28]

Due to dense ionization, heavy ions have increased biological effectiveness in the Bragg peak region, resulting in a reduced cell repair rate. Linear Energy Transfer (LET) is a measure of ionization density. High LET allows for the application of a lower physical dose while maintaining the same biological effect as photons – meaning ions have a higher Biological Effectiveness Factor (BEF).

Another advantage of using carbon ions in treatment is their resistance to hypoxic tumor areas. They are less susceptible to the so-called hypoxic effect, which occurs in tumor areas with limited oxygen access. That means that this therapy may be more effective in treating tumors with a more complex microstructure. An undeniable advantage is also the ability to use PET technology to track the movement of carbon ions in real-time (due to the ability to monitor positron emission). This is extremely important for moving tumors or changing body geometry.

3.5.2 Equipment and System

The equipment for ion-beam radiotherapy at GSI (as seen in Figure 29) is based on:

- SIS-18 Accelerator (responsible for delivery of radiation to the treatment area).
- Raster-scanning as the active beam delivery system, including:
  - Fast energy variation by the accelerator and online quality control including in situ PET diagnosis
  - Single beam-spot treatment planning, including Local RBE assignment according to the tissue and the radiation field.
- Treatment Table (is movable and can be precisely positioned to allow accurate radiation delivery to the targeted area),.

The parameters of the given elements are presented below in Figure 28.

Ion	**Carbon**
Range in tissue	20…300 mm H_2O
Field size	200 mm x 200 mm
Dose range	Treatment volume 0.75 – 4.0 Gye
	Normal tissue < < 2Gye
Treatment time	< 5 min / fraction
Raster Scanner	
Deflection angle	Horizontal 1.45° vertical 3.30°
Radius	12.0 m
Field size	20cm x 20 cm
Scan speed	Horizontal: 2.0 cm/ms vertical 1.0 cm/ms
Field ramp rate	Horizontal: 38.0 T/sec vertical: 9.5 T/sec
Max current	410 A
Rise time	Horizontal:10 ms vertical 40 ms
Accelerator	
Energy range	85- 430 MeV/u (range 20- 300 mm water equivalent)
Energy stepping	255 steps, cycle time 5 sec
Energy definition	0.5 %
Extraction mode	Slow > 2 sec flat top
Extraction interrupt	< 1msec
Intensity range	10** 6 to 10**8 particle / spill
Beam spot size	7 steps: FWHM 4- 10 mm
Beam spot stability	< 20% FWHM, achromatic focusing

Figure 28: Parameters of the GSI therapy system.[29]

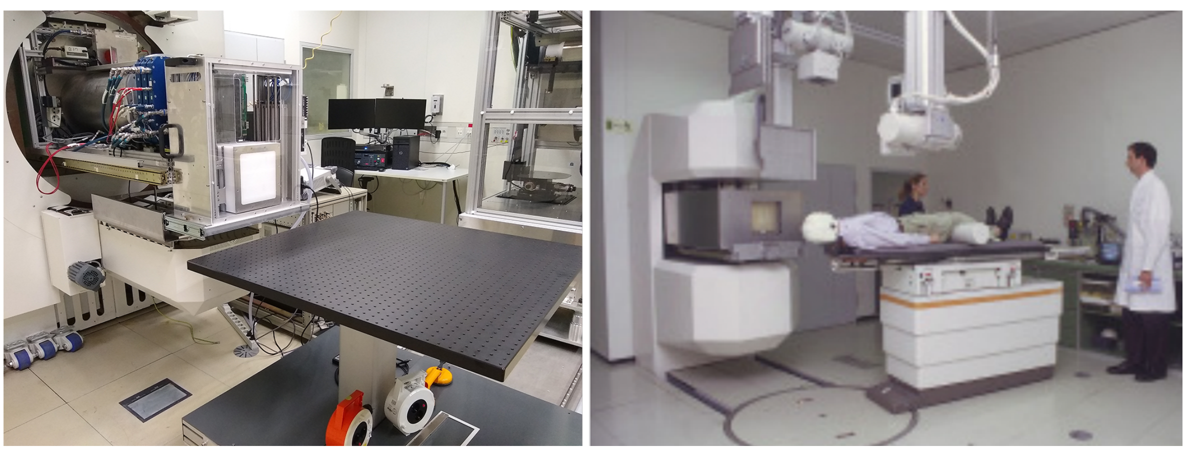

Figure 29: Radiotherapy room at GSI.[30][31]

In radiotherapy, geometric alignment is crucial for each treatment area, known as the Planning Target Volume (PTV). Many techniques allow precise beam delivery. At GSI, raster scanning techniques and the so-called pencil beam have been utilized. **Raster scanning** involves scanning the tumor area with a beam of heavy ions, specifically carbon ions. Each point in the tumor area is scanned, allowing the delivery of appropriately modulated radiation doses tailored to the tumor's shape.

The **pencil beam** is a special type of ion beam, in this case, carbon ions, delivered pointwise. When we think of a pencil, we envision a narrow and focused instrument that can be moved with precision. Similarly, in radiotherapy, the pencil beam technique employs a focused beam of ions, to deliver radiation to the tumor.

In this context, a "single pencil beam" refers to a narrow beam of ions that is delivered to a specific point within the tumor area. It's akin to drawing a line with a pencil, where each stroke of the pencil represents the delivery of ion radiation to a precise location within the tumor volume.

Importantly, while each pencil beam delivers radiation to a specific point, multiple pencil beams are used together to cover the entire tumor volume. This means that the entire ion beam is composed of numerous individual pencil beams, each contributing to the overall radiation dose delivered to the tumor.

The pencil beam is used in scanning techniques where different beam points are scanned along and across the tumor area, enabling precise radiation dose delivery.

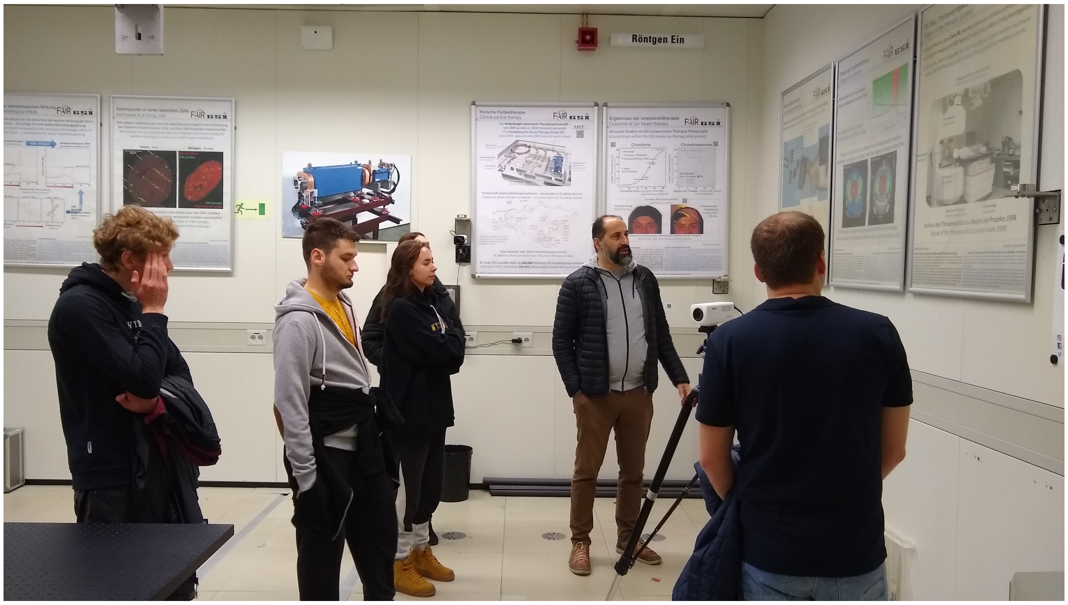

Figure 30: Our group during the visit at GSI radiotherapy room.

3.5.3 Results of the Pilot Project

In the GSI pilot study, approximately 450 patients were treated, primarily diagnosed with tumors of the skull base. The duration of outpatient treatment was approximately 30 minutes each day for 20 consecutive days. The previous treatment, based on an average dose of 60 Gy administered in 20 fractions, was well-tolerated, with no significant side effects reported.

Local tumor control refers to the ability of therapy to eliminate or control tumor growth at its primary site. Meanwhile, **local control probability** is the likelihood of achieving tumor control at the local level with a specific treatment. In both cases, it involves assessing the effectiveness of therapy in preventing tumor growth or recurrence at its primary site.

After three years of observation, a 100% rate of local tumor control was achieved in the case of chondrosarcomas, and 81% in the case of vocal cord tumors. After 5 years from the treatment, tumor growth was stopped in 75% to 90% of patients, depending on the type of tumor. Incidents of adverse events requiring intervention were rare. Based on these promising results, this form of therapy is now widely recognized as an effective medical procedure as seen in Figure 31.

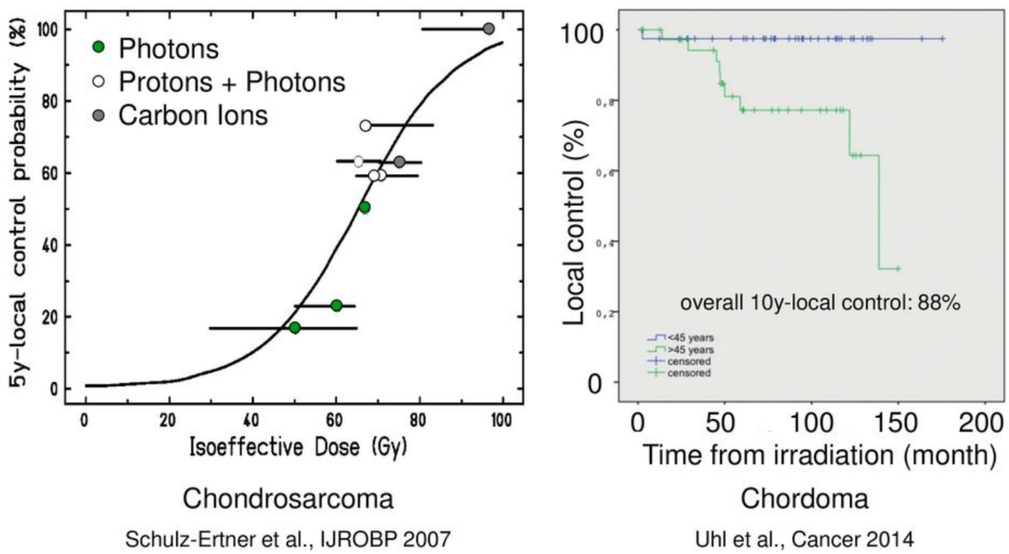

Figure 31: Clinical outcome of the pilot project at GSI for the 5 year local control (right) an percentage local control (left).[32]

Although patient treatments have been transferred to the center in Heidelberg, GSI continues to conduct research on ion and hadron therapies. The innovative approach to treating patients with minimal chances of survival is one of the most significant achievements in the fields of oncology and nuclear medicine. The development of this technology is expected to improve overall cancer treatment outcomes and minimize side effects for patients, especially those presenting unique clinical challenges.

3.6 mCBM

Mini-CBM (shortened to mCBM), installed at the SIS18 facility, is a full system test-setup for Compressed Baryonic Matter (CBM) experiment at FAIR. It allows testing and optimizing performance of detector subsystems under realistic experimental conditions. It will make the commissioning time for CBM at SIS100 significantly shorter. All the members of the CBM collaboration are involved in dedicated mCBM tasks. Said tasks include among others: design of the experimental setup, simulations on benchmark observables, design and construction of the mCBM cave and the beamline. The mCBM detector subsystems, shown in Figure 32 [20], consist of:

- **T0** - provides time-zero measurement,
- **mSTS** - Mini Silicon Tracking System; registers hits from passing charged particles, what allows for track reconstruction and momentum value extraction,
- **mMuCh** - Mini Muon Chamber; detects low-momentum muons,
- **mTRD** - Mini Transition Radiation Detector, helps to identify electrons or positrons and separates them from other charged particles,
- **mTOF** - Mini Time-of-flight Detector; stop detector in T0 − mTOF dual timing measurement system,
- **mRICH** - Mini Ring Imaging Cherenkov; allows clean electron identification based on Cherenkov radiation.

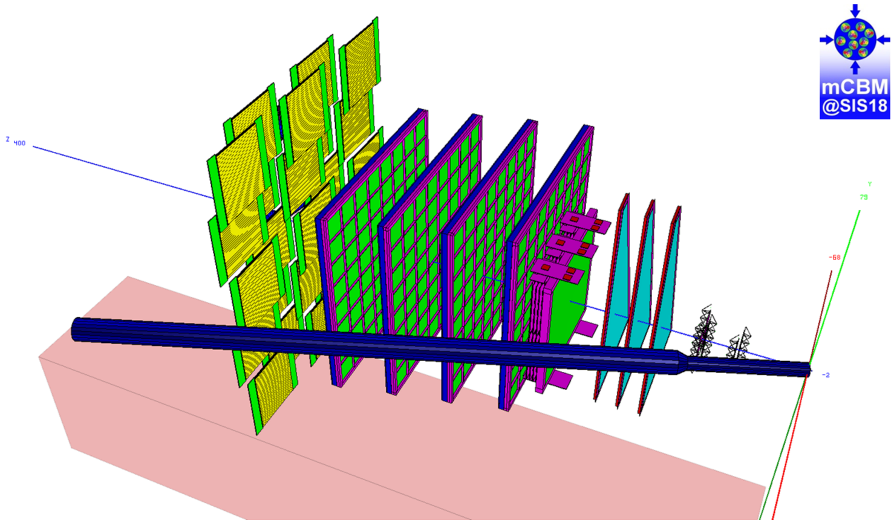

Figure 32: Layout of mCBM detector subsystems.

In 2022 a beam campaign was held for mCBM. During the experiment nickel ions were accelerated to the kinetic energy of 1.93A GeV and were incident on the nickel target. The beam intensity reached up to 10^{10} ions per spill and interaction rate was approximately equal to 400 kHz (see [21] p. 66). Overall, the experiment was deemed successful with an outstanding vertex reconstruction for all possible sensor pairs. It is believed that hit reconstruction efficiency analysis is feasible under certain conditions as mentioned in [21], page 66.

To cope with the high counting rates and track densities of the TOF wall, the Multi-Strip Multi-Gap Resistive Plate Counters (MSMGRPCs) were designed. Their performance was tested during in-beam tests held in mCBM experimental setup. It was assessed that the counters had to be improved. The second prototype was installed and tested during June 2022 mCBM in-beam test campaign. At this time mTOF chambers and MSMGRPCs were exposed to the highest beam intensity ($4 \cdot 10^8$ particles per spill) for 8 hours. The spill shapes were successfully reconstructed, but in 2022 data analysis was still in progress (see [21] p. 125)

3.7 UNILAC

Linear particle accelerators, commonly known as linacs, are a type of facilities that accelerate charged particles along a straight path. This means that, unlike cyclotrons, the beam particles pass through each element only once. Linacs accelerate heavy ions relatively more easily than cyclotrons because they do not require generating a very strong magnetic field. Depending on the energy needed, two types of linear accelerators can be used. We can obtain lower energies by placing a charged particle in a constant electrostatic field. The Van de Graff generator works on this principle. However, accelerators with a high-frequency electric field are much more effective. A representative of this second class of units is UNILAC (Universal Linear Accelerator). It can accelerate various particles, from protons to uranium nuclei up to 0.16 of the speed of light [23].

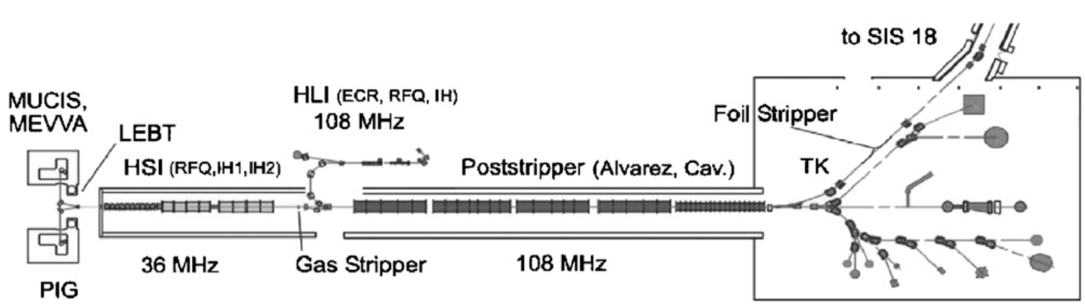

Figure 33: Schematic view of GSI UNILAC [22]

The ions used in the beam can originate from various sources. As shown in Fig. 33, one of them is MEVVA (Metal Vapor Vacuum Arc). In this method metal vapor vacuum arc is used to produce plasma from which the ions are extracted [24]. The second method is MUCIS (Multi Cusp Ion Source) which works on the basis of magnetic confinement of plasma. The third ion source is PIG (Penning Ionization Gauge). It works using high voltage generated between electrodes. The accelerated electrons travel through a chamber filled with low-pressure gas. When they collide with gas molecules, they can ionize them. There are also other ion sources that are not included in Fig. 33 such as CHORDIS (Cold or HOt Reflex Discharge Ion Source), VARIS (Vacuum ARc Ion Source) [25].

The charged particles produced move first to the Low Energy Beam Transport (LEBT). Its tasks are to fully transmit high current beams, preserve brilliance along the beamline, separate isotopes for all the elements. [26].

Figure 34: High Current Injection (HSI) part of UNILAC

The beam then passes to High Current Injector (HSI) shown Fig. 34. At first, it's preaccelerated along RFQ and passes to the Inter-Digital H-type linac. Here particles achieve up to 0.05 speed of light. At this stage, the beam particles are charged only slightly. The beam ions can become charged even more by stripping electrons from them. A gas-filled chamber (Gas Stripper) standing in the path of the low-charged beam is used for this purpose. In the case of ions directed towards SIS 18, they gain even higher charges after the dedicated Foil Stripper [23].

Final acceleration is achieved along a Poststipper (Fig. 35) containing five Alvarez-type cavity drift tubes. In that kind of linacs, an interlaced electric field is applied at a given radio frequency to the entire resonant chamber. The inner tubes are placed inside to protect particles from the decelerating phase of the field oscillation.

After passing through the mentioned UNILAC elements, the beam can be transported to the SIS 18 synchrotron or further for various experimental branches.

Figure 35: Poststripper part of UNILAC.

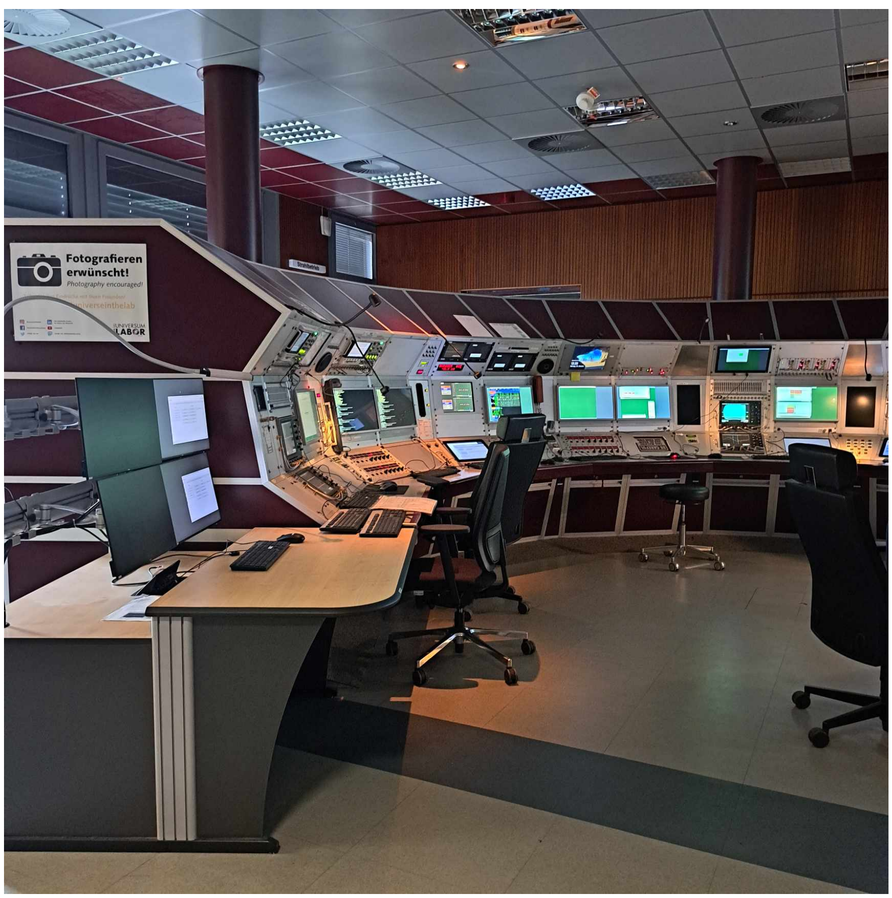

Figure 36: Beam Management Center. Manipulation of beam parameters is still largely done manually.

References

[1] S. Spies (HADES Collaboration), EPJ Web Conf. **259**, 01007 (2022)

[2] A. Rost, *Ph. D. Thesis*, Technische Universität Darmstadt (2020)

[3] P. Chudoba *et al.* (HADES Collaboration), J. Phys.: Conf. Ser. **1667**, 012007 (2020)

[4] P. La Rocca, F. Riggi, Advances in Photodiodes (2011)

[5] M. Wiebusch, *Ph. D. Thesis*, Johann Wolfgang Goethe-Universität in Frankfurt am Main (2019)

[6] B. Franzke, Nucl. Instr. Meth. B, **24**, 18 (1987)

[7] `https://www.gsi.de/en/work/research/appamml/atomic_physics/experimental_facilities/esr`

[8] B. Schlitt *et al.*, Nucl. Phys. A. **626**, 315 (1997)

[9] S. Litvinov, *et al.*, 13th Int. Particle Acc. Conf. IPAC2022 (2022)

[10] D. Winters *et al.* (FAIR Collaboration), Phys. Scr. **2015**, 014048 (2015)

[11] N. Angert *et al.*, Proc. EPAC'88 pp.1436 (1988)

[12] F. Nolden *et al.*, AIP Conf. Proc. **821**, 177 (2006)

[13] G. I. Budker *et al.*, Part. Accel. **7**, 197 (1976)

[14] `https://www.gsi.de/en/researchaccelerators/fair/the_machine`

[15] T. Ablyazimov *et al.* (CBM Collaboration), Eur. Phys. J. A **53**, 60 (2017).

[16] `https://www.cbm.gsi.de/detectors.html`

[17] `https://www.gsi.de/work/gesamtprojektleitung_fair/super_frs/the_super_frs_machine`

[18] `https://www.gsi.de/en/researchaccelerators/research_an_overview/green-it-cube`

[19] `https://hpc.gsi.de/virgo/`

[20] `https://www.gsi.de/work/forschung/cbmnqm/cbm/activities/mcbm`

[21] CBM Progress Report 2022, CBM Collaboration (2022) `https://repository.gsi.de/record/336786/files/CBM-PR-2022.pdf`

[22] W. Barth *et al.* (FAIR Collaboration), Nucl. Instr. and Meth. A **577**, 211 (2007)

[23] `https://www.gsi.de/work/beschleunigerbetrieb/beschleuniger/unilac/unilac`

[24] I. G. Brown, IEEE Trans. Nucl. Sci. **32**, 5 (1985)

[25] `https://www.gsi.de/work/beschleunigerbetrieb/beschleuniger/ionenquellen/sources/ion_sources`

[26] L. Dahl, P. Spädtke, Proc. LINAC'00 (2000)

[27] `https://www.gsi.de/work/forschung/biophysik/forschungsfelder/space_radiation_physics/ion-beam-theray`

[28] `https://www.gleneagles.com.sg/tests-treatments/proton-beam-therapy`

[29] `https://slideplayer.com/slide/11982878/`

[30] https://www.gsi.de/en/start/news/details?tx_news_pi1%5Baction%5D=detail&tx_news_pi1%5Bcontroller%5D=News&tx_news_pi1%5Bnews%5D=5175&cHash=3626858e4430c862cf2ad42de9dd5607

[31] https://www.hzdr.de/FZD/Jahresbericht/2001-2002/Ionenstrahlen.pdf

[32] https://slideplayer.com/slide/11982878/

[33] https://www.blickle.com/products/success-stories/hygiene-medicine-design/success-story-lsdfe-poth

[34] https://www.flickr.com/photos/brookhavenlab/3119988763